ACS Photonics

pubs.acs.org/journal/apchd5

Article

Moiré Effects in Silicon Photonic Nanowires

Tahmid H. Talukdar, Anna L. Hardison, and Judson D. Ryckman*

Cite This: *ACS Photonics* 2022, 9, 1286−1294

Read Online

ACCESS | Metrics & More | Article Recommendations | Supporting Information

ABSTRACT: Photonic moiré lattices offer an attractive platform for manipulating the flow and confinement of light from remarkably simple device geometries. This emerging field draws inspiration from the rapid research progress observed in twisted bilayer van der Waals materials or "twistronics," instead of applying moiré physics to photon propagation in wavelength-scale optical media. However, to date, only a limited number of experimental studies have been performed in this area, and there is strong interest in understanding how moiré effects can be tailored in compact and scalable optical technologies such as an integrated photonics platform. In this work, we map the moiré effects of one-dimensional (1D) photonic moiré lattices composed of width-modulated silicon nanowires, including the construction of a 1D experiment analogous to the twisting of a two-dimensional (2D) lattice. Although the twist angle $\Delta\theta$ and/or lattice mismatch $\Delta\Lambda$ are the sole defining parameters for infinite moiré crystals, we demonstrate how the crystal size, symmetry, and moiré fringe phase $\Delta\phi$ also serve as important degrees of freedom. Through tailoring these parameters, we map a wide range of behaviors including the formation of moiré photonic crystal cavities, the onset of miniband formation and operation as a coupled resonator optical waveguide (CROW), widely tunable Q-factors and group velocities, suppression of grating sidebands, and persistent vs extinguishable tunneling. These results provide insight into the moiré physics of 1D optical systems and highlight various operating regimes relevant to the design of finite photonic moiré lattices and devices.

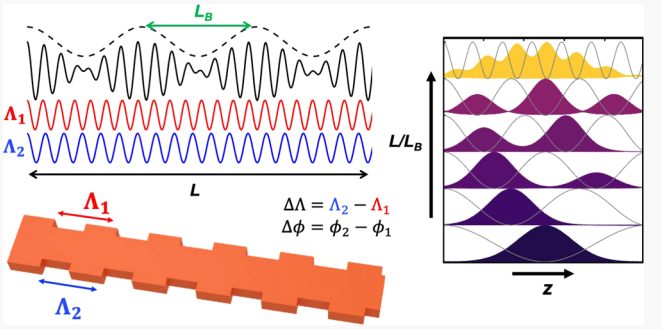

KEYWORDS: *moiré lattices, nanophotonics, photonic crystals, quasi-crystals, resonators, waveguides*

INTRODUCTION

Recently, moiré lattices of bilayer van der Waals materials have attracted significant research interest due to their distinct physics, novel properties, and prospective opportunities for "moiré engineering". Owing to the novel material properties that may originate from stacked van der Waals materials and the precise twist angle $\Delta\theta$ between layers, as illustrated in Figure 1a, research in this area is often referred to as "twistronics" or "twist-optics". These emergent fields have led to discoveries that include controlling electronic band properties,[1] magic-angle superconductivity,[2] moiré excitons,[3] emergence of insulating states[4] and ferromagnetism,[5] as well as polaritonic moiré effects and nanoscale light manipulation in multilayer van der Waals materials.[6,7] Beyond van der Waals materials, we should also expect moiré physics to yield similarly novel properties and technological opportunities in optical analogues[8]—i.e., moiré lattices defined in wavelength-scale photonic media. Compared to van der Waals material systems that are constrained by fixed lattice dimensions and delicate twist angles, photonic systems offer enormous freedom and control over moiré lattice parameters thanks to the availability of mature on-demand patterning. This makes photonic structures especially well suited for both investigating moiré effects and harnessing moiré effects in scalable optical technologies.

Recent works involving 2D moiré lattices in the photonic domain have now demonstrated a 2D localization−delocalization transition alongside flat-band physics,[9] optical soliton formation,[10] magic-angle resonant lasers,[11] microwave regime effective gauge fields,[12] and novel types of Fourier surfaces[13,14] and metasurfaces.[15,16] Moiré patterns are not restricted to 2D formats and can be realized in 1D lattices, as illustrated in Figure 1b. Along this vein, several works have recently reported experiments relating to 1D moiré photonic lattices, or the bichromatic lattices first conceptually described by Aubry and André[17] and Harper,[18] including demonstrations of highly tailorable optical filters,[19] high Q-factor photonic crystal cavities,[20−22] and physically unclonable quasi-crystal interferometers.[23] In this context, the concept of a twist angle can be replaced with a one-dimensional lattice mismatch parameter $\Delta\Lambda = \Lambda_2 - \Lambda_1$, where $\Lambda_2 > \Lambda_1$. For a sufficiently large lattice mismatch, a comparatively trivial operating regime may exist,

Received: November 25, 2021
Published: March 10, 2022

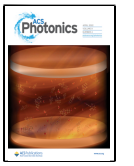

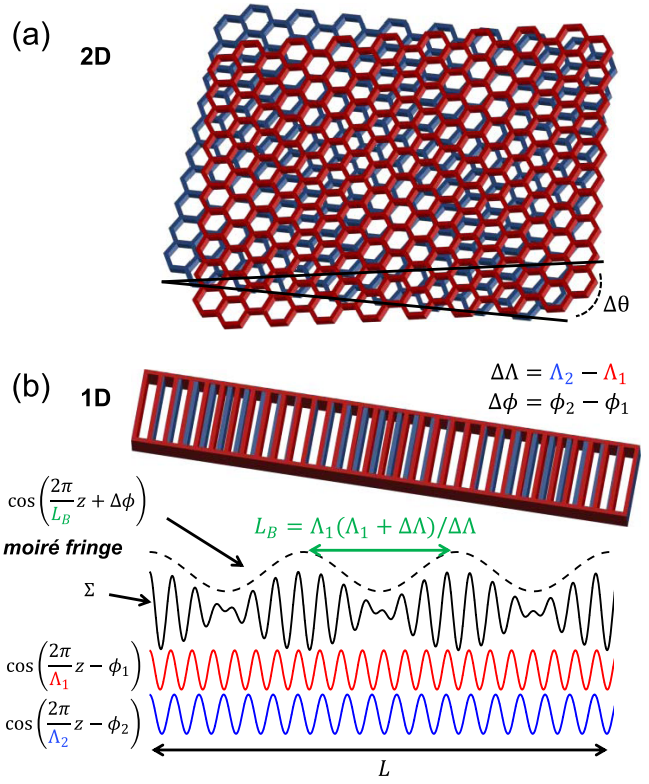

Figure 1. Illustration of moiré lattice formation in (a) 2D systems with a slight twist in angle $\Delta\theta$ and (b) 1D systems with a lattice mismatch $\Delta\Lambda = \Lambda_2 - \Lambda_1$ and finite device length L. The resulting moiré fringe pattern is characterized by a beat length L_B and an initial phase $\Delta\phi$ derived from the superposition of two sublattices with individual periods Λ_1 and Λ_2.

where the local band structure directly reflects that of each sublattice, effectively providing a superposition of multiple Bragg peaks.[24] However, for sufficiently small to moderate lattice mismatch values, nontrivial transport and localization effects can arise owing to the formation of a wavelength-scale moiré fringe pattern, which coincides with the formation of wavelength-scale effective potential wells. Yet to our knowledge, no prior work has systematically investigated, in 1D optical nanowires, an experiment analogous to the twisting of a 2D moiré lattice, nor has sufficient attention been paid to the nuanced operation of finite-length structures, wherein the crystal length, symmetry, and relative phase $\Delta\phi = \phi_2 - \phi_1$ between sublattices also play crucial roles in dictating behavior.

In this work, we study light transport in 1D moiré lattices of width-modulated silicon photonic nanowires and construct an experiment that serves as a 1D analogue to twist angle experiments in 2D systems. In addition, we examine the effects of skewing the lattice mismatch $\Delta\Lambda$ and relative phase $\Delta\phi$ between sublattices in finite-length moiré lattices. Freedom over these two simple parameters, in addition to the selection of the device length and grating type/symmetry, are shown to provide enormous freedom in spectrally tailoring optical transport and confinement.

Approach. As illustrated in Figure 1b, the superposition of two sublattices creates a moiré fringe pattern that oscillates on a longer scale, with a beat length $L_B = \Lambda_1\Lambda_2/\Delta\Lambda$. The moiré fringe pattern defines the arrangement of effective moiré potential wells, with the maximum number of complete wells residing in a finite crystal length, L, corresponding to the number of beat lengths residing in the structure, $N = L/L_B$. It should be noted that a beat length can be defined regardless of the exact periodicity vs aperiodicity of the underlying structure. Note: for sublattices exhibiting an irrational value for Λ_1/Λ_2, the device is quasi-crystalline and exhibits Aubry−André analyticity breaking owing to the lack of Bloch periodicity,[17] whereas a structure exhibiting a rational value for Λ_1/Λ_2 is deemed super-periodic. However, these distinctions may lose significance in many practical instances since compact finite-length structures with rational Λ_1/Λ_2 may remain too short to exhibit their periodic translational symmetry. Furthermore, the existence of the beat length does not necessarily indicate or require an exactly periodic refractive index profile but is suggestive of an approximately periodic effective potential.[25]

In this study, we consider 1D light propagation in width-modulated silicon nanowires operating near the wavelength 1550 nm. For a quasi-TE polarized silicon nanowire waveguide with a width of 500 nm the nominal propagation constant, $\beta = 9.9\ \mu m^{-1}$, leads to a Bragg period near 317 nm. In the case of a moiré lattice defined with sublattice periods $\Lambda_1 = 317$ nm and $\Lambda_2 = 318$ nm, or a lattice mismatch $\Delta\Lambda = 1$ nm, the beat length L_B and size of a single effective potential well are $\sim$100 μm. In this work, we primarily consider structures with finite crystal length, $L = 100\ \mu$m, and systematically vary the lattice mismatch $\Delta\Lambda$ or initial phase $\Delta\phi$. With this approach, we probe several general regimes including: (i) $L < L_B$, (ii) $L = L_B$, and (iii) $L > L_B$. To form our 1D moiré photonic nanowires, we superimpose two sublattices with periods Λ_1 and Λ_2 using two distinct design types:

- Type-A: asymmetric sidewall modulation. The sublattices are applied asymmetrically to either side of a sidewall modulated silicon nanowire as shown in Figure 2a. An SEM image of a fabricated type-A design is shown in Figure 2b. The type-A structure lacks mirror symmetry similar to asymmetric phase-shifted Bragg gratings.[26] This produces a three-level moiré lattice composed of narrow (low), moderate, and wide (high) nanowire (effective index) segments, which is further illustrated in Figure S2. As such, the partial reflection amplitude at each sequential interface does not consistently alternate between positive and negative as in a traditional binary crystal. We note that the type-A geometry has recently been harnessed in specially chirped moiré lattices to construct highly tailorable optical filters,[19] and a related waveguide structure involving a two-step etch has also been theoretically examined.[27] In our design, the duty cycle of each sublattice grating is fixed to 50%.
- Type-B: symmetric sidewall modulation. The sublattice periods are applied symmetrically to both sides of the sidewall modulated silicon nanowires. The sublattices are generated independently with 50% duty cycles, then superimposed, and the final type-B moiré grating, as illustrated in Figure 2d, is defined by performing a Boolean "AND" operation, which yields a binary crystal with grating teeth at the intersection of both sublattices. The corresponding SEM image of an example type-B design is shown in Figure 2e. This design maintains mirror symmetry and naturally produces variations in the width and spacing of the grating teeth along the propagation direction. In a separate work, our group has employed a modified form of this grating type, with smaller grating teeth and a spiral format, to synthesize quasi-crystal interferometers for physical unclonable function.[23]

https://doi.org/10.1021/acsphotonics.1c01800
ACS Photonics 2022, 9, 1286−1294

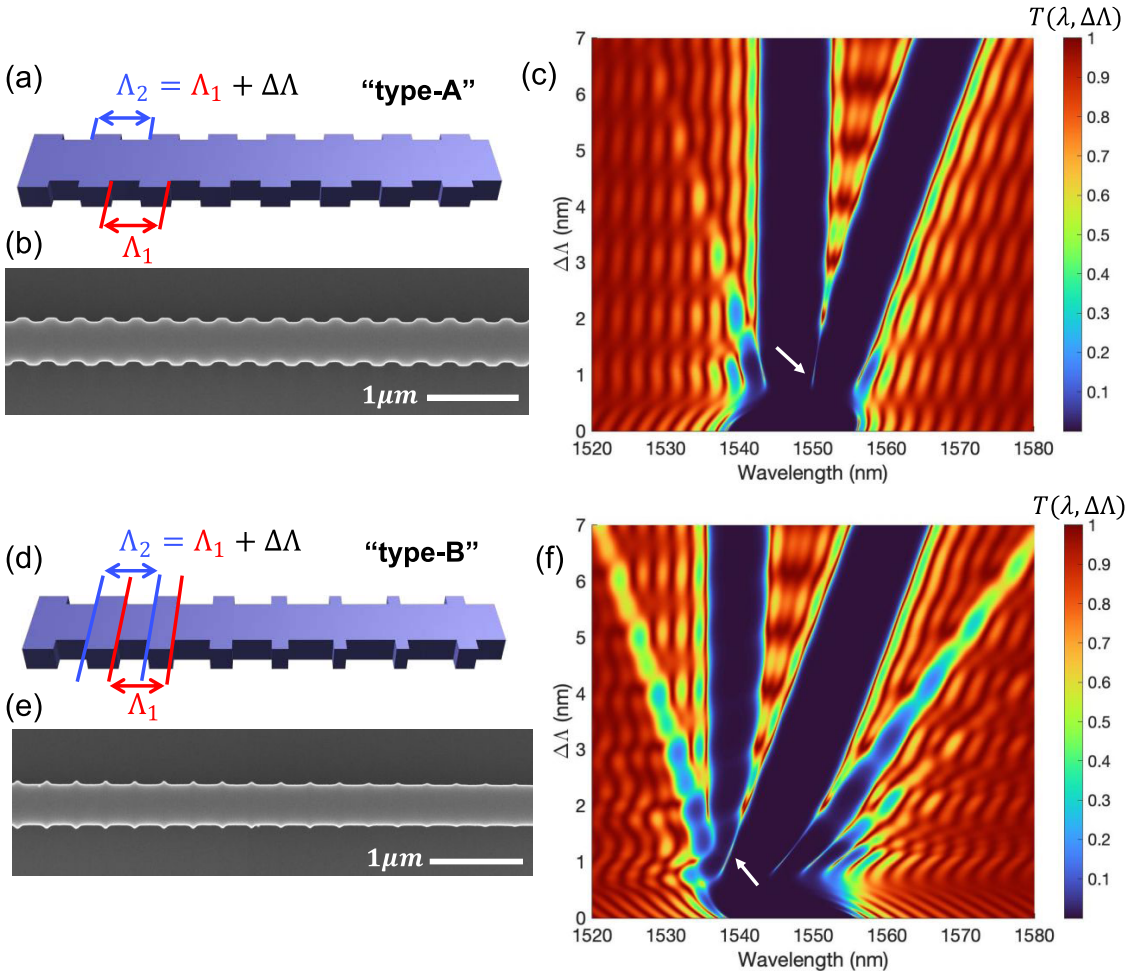

Figure 2. Illustration of the (a) type-A nanowire, (b) an example SEM image after fabrication, and (c) modeled transmission spectra vs lattice mismatch for $\Delta\Lambda$ skewed from 0 to 7 nm. Illustration of the (d) type-B nanowire, (e) an example SEM image after fabrication, and (f) modeled transmission spectra for the same lattice mismatch range considered for the type-A nanowire for $\Delta\Lambda$ skewed from 0 to 7 nm. The other parameters are fixed to $\Lambda_1 = 317$ nm, $\Delta\phi = 0$, and $L = 100\ \mu$m. The white arrows in (c) and (f) indicate the fundamental mode moiré resonance associated with $\Delta\Lambda = 1$ nm, where $L = L_B$.

We model light transport in both types of moiré photonic nanowires using a dispersive transfer matrix method, which also accounts for a nominal ~2.5 dB/cm propagation loss of standard silicon nanowires (see the Methods section). Using this approach, we directly model their transmission and modal characteristics, e.g., spectral response, group index, and electric field distribution. Type-A and type-B moiré photonic nanowires were then fabricated in a standard 220 nm silicon-on-insulator (SOI) platform and characterized by collecting grating coupled transmission spectra near 1550 nm (see the Methods section).

RESULTS AND DISCUSSION

In Figure 2c,f we present the predicted transmission characteristics of type-A and type-B waveguides for lattice mismatch values over the range $\Delta\Lambda = 0-7$ nm, where $\Delta\phi = 0$. For the trivial case of $\Delta\Lambda = 0$, each structure acts as a conventional Bragg grating with a measured coupling coefficient "kappa" of ~9.5×10^3 cm^{-1}. Note: transmission spectra of typical Bragg structures with $\Lambda = 317-324$ nm can be found in Figure S1. As the lattice mismatch $\Delta\Lambda$ is increased to ~0.5 nm, both structures function as apodized gratings with characteristic side-lobe suppression. In this regime, the crystal already lacks translational symmetry, while the effective moiré potential does not yet form a complete well owing to $L < L_B$. Then, near $\Delta\Lambda \approx 1$ nm, a transition occurs where cavity resonances are formed due to $L > L_B$ and $N > 1$ such that at least one complete moiré potential well exists inside the finite-length crystal. Despite the overlapping bandgaps of each sublattice, transmission through the crystal is mediated by input/output coupling to resonant modes formed by the moiré potentials. For example, at $\Delta\Lambda = 1$ nm, the type-A structure defines a moiré photonic crystal cavity, with the fundamental resonance, indicated by the white arrow in Figure 2c, exhibiting a quality (Q) factor of ~40k. The type-B structure meanwhile supports a multiply resonant moiré photonic crystal cavity, which we discuss in greater detail upon introducing Figure 3.

Notably, the type-B structure examined in Figure 2d shows clear signatures of both first-order Bragg reflection and sidebands related to the spatial frequency of the moiré fringe pattern, both of which suppress transmission by coupling the forward propagating wave, $\beta > 0$, with the reverse propagating wave, $\beta < 0$. The generalized phase matching condition for Bragg reflection attributable to our moiré lattice occurs when

$$2|\beta| = mG_1 + nG_2 = m\frac{2\pi}{\Lambda_1} + n\frac{2\pi}{\Lambda_2} \quad (1)$$

https://doi.org/10.1021/acsphotonics.1c01800
ACS Photonics 2022, 9, 1286−1294

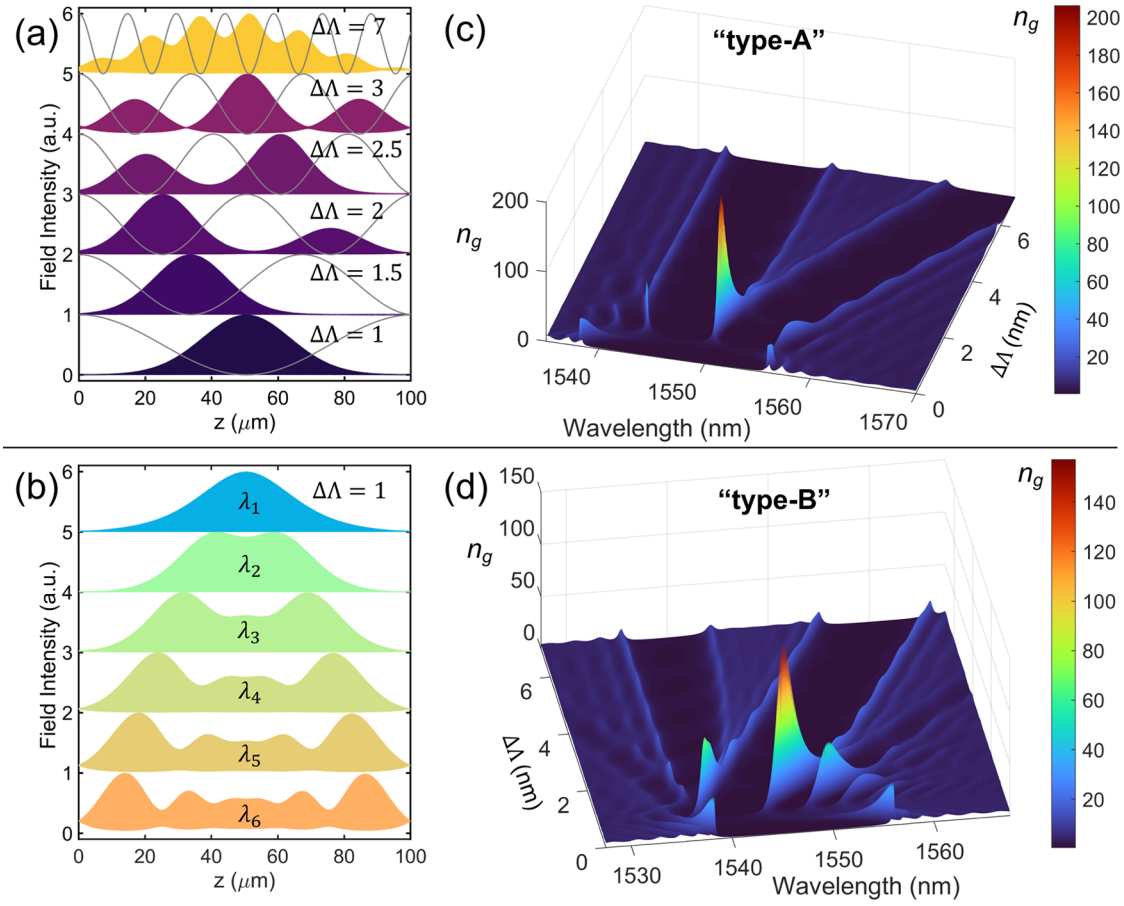

Figure 3. Mode distribution and group indices of moiré photonic nanowires. Electric field intensity for (a) type-A devices with varying ΔΛ, superimposed with the corresponding moiré fringe pattern, and (b) resonant modes of the type-B structure, where ΔΛ = 1 nm. (c) Simulated group index map vs lattice mismatch for type-A and (d) type-B structures. Resonant mode wavelengths in (a) were chosen from transmission resonances in Figure 2a, and for N >2, the shortest-wavelength resonant supermode is shown.

where G_1 and G_2 describe the grating wavenumber $2\pi/\Lambda_1$ and $2\pi/\Lambda_2$ for each sublattice, where m and n are integers.[28,29] In addition to the Bragg peaks associated with $(m,n) = (+1,0)$ and $(0,+1)$, the next most prominent features of Figure 2d are reflection sidebands consistent with $(m, n) = (+2,-1)$ and $(-1, +2)$, respectively. These sideband reflection peaks are a form of spatial frequency mixing, which provide a net wavenumber described by either $2G_1 - G_2 = G_1 + \Delta G$ or $2G_2 - G_1 = G_2 - \Delta G$, where $\Delta G = 2\pi/L_B$ describes the spatial frequency of the fringe pattern. Notably however, these sideband signatures are comparatively suppressed by the type-A moiré lattice and do not appear in Figure 2c. In principle, cancellation of either ΔG sideband can occur if, for each partial reflection contributing to this spatial frequency, there is another partial reflection with equal amplitude and opposite phase. The observation of this effect only in the type-A design is attributed to its broken mirror symmetry and three-level moiré lattice composed of narrow, medium, and wide segments. As detailed in Figures S2 and S3, the type-A moiré lattice contains an additional series of multiperiodic partial reflections that are phase-delayed relative to the reflections shared in common with the type-B lattice, coinciding with a suppression of the ΔG Fourier component of the grating's $n_{eff}(z)^2$ profile.

Figure 3 presents the simulated modal characteristics of type-A and type-B moiré photonic nanowires. In Figure 3a, we examine the electric field intensity distribution for resonant modes associated with the moiré potentials of type-A structures where $\Delta\Lambda = \{1, 1.5, 2, 2.5, 3, 7\ (\text{nm})\}$, and correspondingly, $N = L/L_B \approx \{1, 1.5, 2, 2.5, 3, 7\}$. These modes were chosen from transmission resonances in Figure 2c and correspond to $\lambda_0 = \{1550.12, 1550.725, 1551.2, 1551.66, 1552.6, 1552.75\ (\text{nm})\}$. It is evident that light is localized by the formation of moiré potential wells. The locations of the moiré wells are visualized by the moiré fringe patterns depicted in Figure 3a. The depth and density of the wells dictate how strongly their modes couple with adjacent wells and/or the input/output waveguides. For example, both $N = 1$ and $N = 1.5$ contain only a single effective potential well. However, the resonant transmission through the structure, from Figure 2c, is near unity for the $N = 1$ structure owing to the symmetric input/output coupling configuration, whereas the $N = 1.5$ structure exhibits significantly lower transmission due to undercoupling at the output.[30] This phenomenon repeats for integer values of N, regardless of crystal type, and could be interpreted as a magic-length effect. Under this magic-length condition, maximum resonant transmission through the crystal is observed, e.g., Figure 2c, when $L = NL_B$ assuming $\Delta\phi = 0$, i.e., the moiré crystal length equals an integer number of beat lengths and naturally exhibits symmetric input/output coupling.

In Figure 3b, we examine the electric field intensity distribution for resonant modes associated with the moiré potential of the type-B structure, where $\Delta\Lambda = 1$ nm, and correspondingly $N = L/L_B = 1$. This structure is found to support multiple resonances, with a fundamental mode at $\lambda = 1538.175$

https://doi.org/10.1021/acsphotonics.1c01800
ACS Photonics 2022, 9, 1286−1294

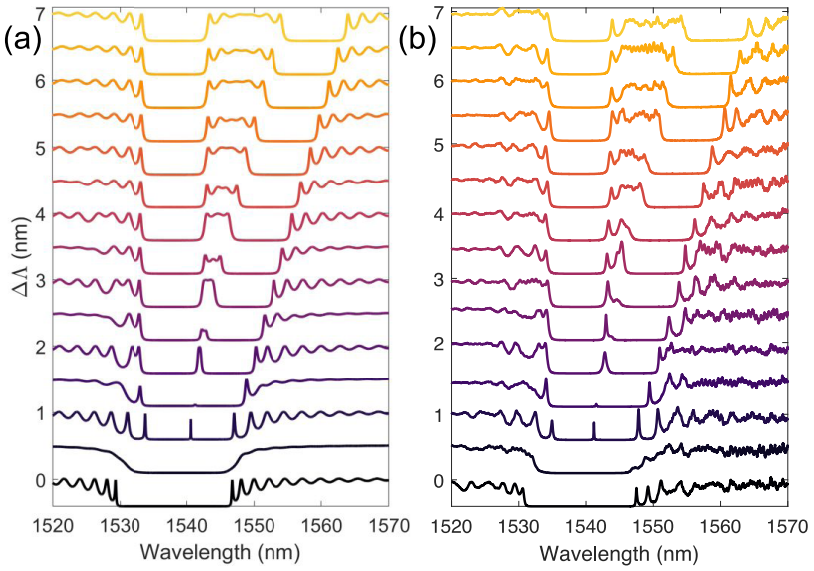

Figure 4. Transmission spectra of finite-length type-A devices showing a comparison between (a) theory and (b) experiment for varying $\Delta\Lambda$, where Λ_1 = 317 nm, $\Delta\phi = 0$, and L = 100 μm. The model in (a) accounts for the experimentally realized waveguide dimensions.

nm (white arrow of Figure 2f) and higher-order modes ranging from 1545 to 1560 nm. Given that the resonant frequency decreases with increasing mode order, this moiré lattice defines a valence or dielectric band type cavity with alternating symmetric and antisymmetric modes.[31,32] These findings are therefore distinct from but related to the multiresonant conduction or airband-type cavities, which have recently been demonstrated in bichromatic 2D photonic crystals where the resonant frequency increases with increasing mode order.[21] As noted in ref 21, the frequency spacing between each resonant mode is controlled by the shape of the potential well and recent demonstrations in the 2D PhC platform have sought to achieve harmonic (parabolic) potentials to obtain uniform frequency spacing for applications such as comb filters or low-mode-volume optical parametric oscillators.[22,33] In our case, however, we observe that the moiré potential formed in our type-B nanowires does not naturally approximate a parabolic potential since the resonant frequencies are not naturally uniformly spaced. Instead, the frequency spacing shown in Figures 2f and 3b decreases with increasing mode order, as predicted for a cosine-shaped effective potential well.[21] However, our experimental results, to be discussed below, provide insight into how such dielectric band structures can be modified to better approximate a harmonic potential if so desired.

Increasing the lattice mismatch to $\Delta\Lambda > 2$ nm and beyond, the moiré potential enters a regime where $N > 2$, resulting in a cascaded series of coupled moiré cavities. In this regime, we observe the formation of supermodes associated with the coupling between modes of each moiré potential well, as shown in Figure 3a. In such structures, light transport can be described according to a tight-binding or coupled resonant optical waveguide (CROW) description rather than a Bloch representation.[34] Operation of the moiré crystal as a CROW leads to miniband formation, the onset of which is observable in Figure 2a,b, and yields high transmission states that can tunnel through an otherwise insulating crystal.[35] The dispersion relation for the spectrally isolated miniband formed inside the band gap of an infinitely long CROW can be expressed as

$$\omega(k) = \omega_0 + \Delta + \Gamma(\omega)\cos(kL_B) \quad (2)$$

where ω_0 is the resonant frequency of the moiré well, Δ is the frequency difference between ω_0 and the center of the CROW miniband, and $\Gamma(\omega)$ is the frequency-dependent coupling rate between adjacent moiré resonators.[36] For high-Q individual cavities where the coupling is weak, the dispersion and group velocity of such structures, $v_g = \frac{d\omega}{dk} = -\Gamma(\omega)L_B\sin(kL_B)$, can be driven toward zero to achieve flat-band transport.[34,37] Such flat-band features are a hallmark of magic-angle effects such as those demonstrated in bilayer van der Waals materials[2] or wavelength-scale photonic analogues.[8,11] This highlights the closely related group velocity characteristics of 1D and 2D moiré lattices, which in the photonic domain draw direct analogy to 1D CROWs[34] and 2D coupled resonator superlattices.[38] The CROW-like transmission and group velocity characteristics of type-A and type-B structures with varying L and N are further illustrated in Figures S4 and S5. In the present study, however, we primarily consider finite structures where N is small. To predict the group velocity or group index, $n_g = c/v_g$, of finite-length type-A and type-B moiré photonic nanowires, we apply the transfer matrix method (see the Methods section). In addition to providing an indication of the group delay for transmission through the moiré crystal, the group index is proportional to the density of modes[39] and provides an indication of which modes promote the strongest light−matter interactions.

In Figure 3c,d we present the simulated group index of type-A and type-B moiré photonic nanowires. These results correspond to the predicted transmission characteristics of Figure 2 and again consider finite L = 100 μm structures with varying $\Delta\Lambda$. The simulation of the type-A device shows an extraordinarily high group index, n_g ~200, associated with the $\Delta\Lambda$ = 1 nm magic-mismatch moiré cavity (Figure 2c). For $\Delta\Lambda$ = 2 nm and beyond, the group index remains enhanced relative to a nominal waveguide (n_g ~4.2) but reduces to n_g ~20 and lower owing to the lower Q-factor associated with each individual moiré resonator. Similar results are displayed in Figure 3d for the multiresonant type-B devices. Notably, resonant modes residing inside the band gap region display significantly higher group index than band-edge modes. Further enhancements to the

https://doi.org/10.1021/acsphotonics.1c01800
ACS Photonics 2022, 9, 1286−1294

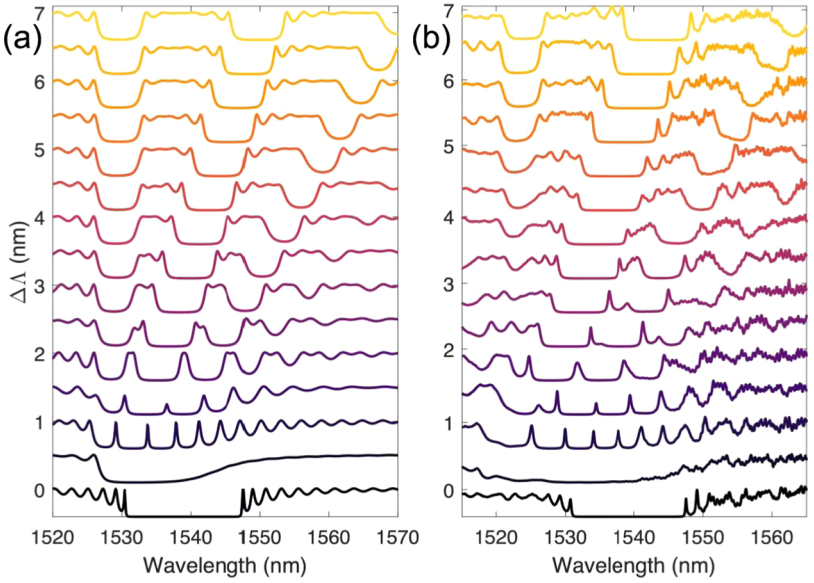

Figure 5. Transmission spectra of finite-length type-B devices showing a comparison between (a) theory and (b) experiment for varying $\Delta\Lambda$, where $\Lambda_1 = 317$ nm, $\Delta\phi = 0$, and $L = 100\ \mu$m. The model in (a) includes a nonuniform fabrication induced distortion to the experimentally realized waveguide dimensions using an "advanced bias" as detailed in Figure S6.

density of modes and group indices could be achieved by intentionally engineering the Q-factor of individual moiré resonators.

Figures 4 and 5 report the experimentally measured transmission of type-A and type-B devices, respectively, alongside a modified simulation accounting for the experimentally realized waveguide dimensions of 460 nm with ±45 nm sidewall modulation (see the Methods section). In this experiment, $\Lambda_1 = 317$ nm is kept constant, and a period skew is performed on Λ_2 from 317 to 324 nm in 0.5 nm intervals, for a $\Delta\Lambda$ skew of 0−7 nm in 0.5 nm intervals. The sublattices are in-phase at the start of the moiré crystal, e.g., $\Delta\phi = 0$. For the type-A geometry depicted in Figure 4, we find that the theoretical prediction and experimental results are in general agreement with one another. This includes the formation of a moiré cavity at $\Delta\Lambda = 1$ nm, with a sharp resonance peak having a Q-factor of ∼25k. This cavity is realized solely by the natural moiré potential, without the need for any targeted system apodization or tapering. We note that such a cavity is easy to design, requiring only $L = L_B$ and $\Delta\phi = 0$, and that the operating wavelength and Q-factor should depend on the choice of Λ_1 and L, respectively. The onset of miniband formation and CROW-like transmission behavior can be seen from $\Delta\Lambda = 2$ nm and beyond. This region does however exhibit experimental fluctuations in transmission which deviate from simulation and is indicative of enhanced sensitivity to fabrication disorder, consistent with conventional CROWs. We expect that similar fabrication disordering of moiré resonances is likely to be observed in 2D magic-angle systems, which can be viewed as moiré-based 2D coupled cavity arrays.

The experimentally measured transmission spectra of type-B devices, as reported in Figure 5b, deviate noticeably from our originally modeled predictions from Figure 2f. Upon close examination of the devices and SEM images of the grating profile, we identified the key source of discrepancy as the fabricated critical-dimension (CD) bias systematically reducing the width and length of the narrow grating teeth. These findings indicate that the type-B design is inherently more fabrication-sensitive than the type-A geometry as some grating teeth are too narrow to be fabricated as designed owing to the nonuniform width of grating teeth and the smaller CDs involved in the structure. This provides some insights relevant to disorder-sensitive applications of such devices, e.g., for realizing disorder-induced localization−delocalization transitions or physical unclonable function, which likely benefit from smaller nanoscale features.[23] As the grating teeth of the type-B design is narrow in size, the impact of the CD bias becomes more apparent, and this produces a non-negligible modulation to the waveguide width profile, $w(z)$, as detailed in Figure S4. Figure 5a presents simulations that account for such a systematic CD biasing effect. The impact of this modulation is a gradual change in the shape of the effective moiré potential, as observed through its effect on the $\Delta\Lambda = 1$ nm multiresonant spectrum. Here, both the experimentally realized results of Figure 5b and the CD bias-modified simulation of Figure 5a show a substantially more uniform frequency spacing between resonances than is predicted for structures with no systematic CD biasing effect as reported in Figures 2f and 3d. The results suggest that gradual width modulations, applied either by process or by design, can be utilized to further tailor or fine-tune moiré potentials to achieve desired properties, e.g., for realizing customized spectral filters or harmonic resonators.[21,22] In other words, additional engineering and/or customization of the moiré lattice is another available design vector, which is readily accessible in wavelength-scale photonic media.

Finally, we experimentally studied the effect of modulating the initial phase $\Delta\phi$ of the moiré fringe pattern as defined in Figure 1b and reported in Figure 6. In this experiment, $\Delta\phi$ is modulated between 0 and 2π by translating the Λ_2 sublattice by an increment Δz between 0 and $\Lambda_2 = \Lambda_1 + \Delta\Lambda$ for three separate type-A designs: $\Delta\Lambda = 0.5$, 1 and 2 nm. As we have previously observed in Figures 2 and 4 for the case $\Delta\phi = 0$, initially the $\Delta\Lambda = 0.5$ nm lattice mismatch device behaves as an apodized grating and produces no resonant cavity modes because a moiré potential well does not form within the full length of the crystal. By applying a phase shift however, we find that it is indeed possible to achieve a lower Q-factor resonant cavity with $\Delta\Lambda = 0.5$ nm. This occurs despite the crystal length L being

https://doi.org/10.1021/acsphotonics.1c01800
ACS Photonics 2022, 9, 1286−1294

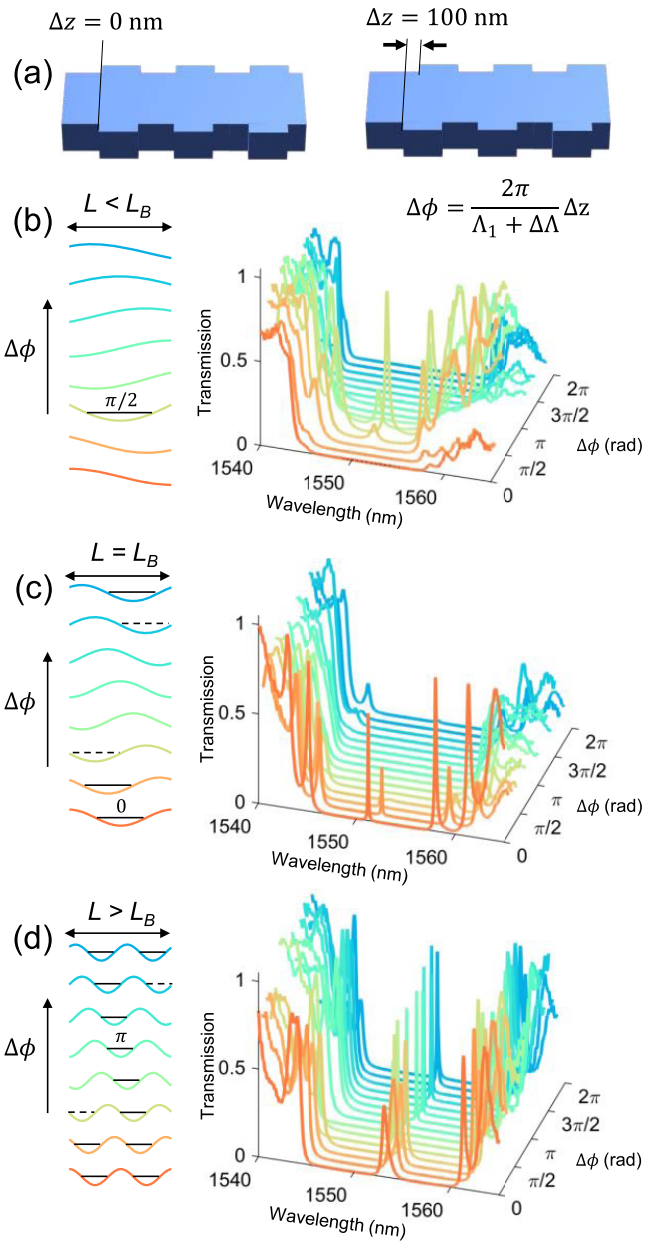

Figure 6. Modulating the moiré fringe phase $\Delta\phi$ in finite nanowires with varying lattice mismatch. (a) Illustration of the phase modulation scheme as applied to a type-A structure. Visualization of the moiré fringe pattern serving as an effective potential (left) and experimental transmission spectra vs phase shift (right) for: (b) $\Delta\Lambda = 0.5$ nm, (c) $\Delta\Lambda = 1$ nm, and (d) $\Delta\Lambda = 2$ nm. In this experiment, $L = 100$ μm and $\Lambda_1 = 317$ nm. Experimental results agree with predictions detailed in Figure S7.

shorter than the moiré beat length L_B and is attributed to the phase shift $\Delta\phi \approx \pi/2$ pushing a shallow potential well into the middle of the finite-length crystal as illustrated by the moiré fringe patterns in Figure 6b. Conversely, it is also possible to push a potential well out of the crystal by applying a sublattice phase shift, as observed for the case where $\Delta\Lambda = 1$ nm and $L = L_B$. Initially, for $\Delta\phi = 0$, there is a resonant transmission peak that corresponds to an integer number of complete moiré wells, residing inside the crystal. As the phase is shifted however, the moiré fringe pattern translates along the optical axis and the effective moiré potential well shifts through the boundary of the crystal. Small phase shifts initially suppress the resonant transmission owing to a lack of symmetric input/output coupling, then as the phase shift increases, the resonances are fully extinguished as the fringe profile and effective moiré potential no longer support a well with a defined local minimum within the finite-length structure. For $\Delta\Lambda = 2$ nm in Figure 6d however, the resonant transmission through the structure is persistent and cannot be extinguished by varying the phase. In this device, transport is mediated by at least one and at most two moiré potential wells owing to the crystal length L equaling twice the beat length L_B. While the resonant transmission in this case remains elevated for any fringe phase, the Q-factor is theoretically predicted and experimentally observed to be tunable with $\Delta\phi$ and maximized for $\Delta\phi \approx \pi$ as shown in Figure 7.

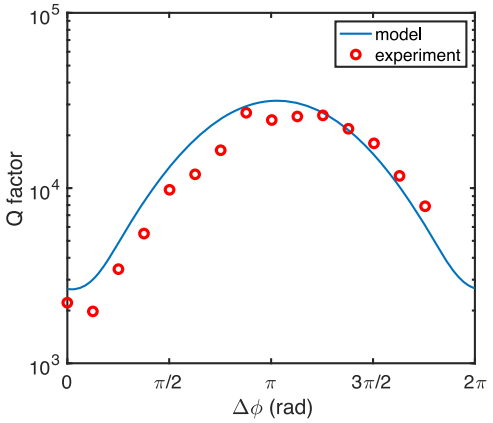

Figure 7. Experimentally measured Q-factor vs moiré fringe phase for the resonance depicted in Figures 6d and S7, where $\Delta\Lambda = 2$ nm, $\Lambda_1 = 317$ nm, and $L = 100$ μm.

The experimental results observed in Figures 6 and 7 highlight a key aspect of finite moiré lattices, i.e., the strong influence that the phase of the moiré fringe plays in dictating transport. While in theoretically infinite-sized structures only magic-angle or magic-mismatch effects arise, in finite structures, we observe the introduction of moiré effects associated with crystal length and phase. Altogether, this expands the magic-angle or mismatch moiré effects to a family of angle, mismatch, length, and phase effects. In practice, this means that the desired design or operating characteristics of a particular device cannot be defined solely through any one of these parameters alone, but rather should be defined while also choosing or constraining the remaining degrees of freedom.

In summary, we theoretically and experimentally examined moiré effects in wavelength-scale photonic structures formed from 1D lattices defined in sidewall-modulated silicon photonic nanowires. This 1D configuration allowed us to study some of the basic, yet nuanced, phenomena associated with wave transport and trapping in moiré potentials. Beyond exploring a 1D analogy to the magic-angle effects observed in 2D systems, we highlight a broader range of moiré effects that are associated with finite-sized structures. These effects span multiple degrees of freedom, including angle, lattice mismatch, fringe phase, and device size or length. A rich variety of operating characteristics are observed to originate from very straightforward device designs, ranging from slow-light and high Q-factor moiré resonators strongly coupled to the feeding waveguide, to moiré-based CROWS, multiresonant filters, suppression of grating sidebands, persistent vs extinguishable transmission, and readily

https://doi.org/10.1021/acsphotonics.1c01800
ACS Photonics 2022, 9, 1286−1294

tunable Q-factors and group velocities. These findings highlight photonic moiré lattices as a promising avenue for continued innovation in integrated optics, especially for classical or quantum optical applications, which may benefit from their combination of simplicity, versatility, compactness, and potential for enhanced light−matter interactions.

METHODS

Device Modeling. We model the transmission characteristics and electric field distribution of the sidewall-modulated silicon nanowires using the transfer matrix method.[40] For this, we first model the waveguide-effective indices as a function of wavelength and waveguide width using a commercial mode solver (Lumerical MODE). Then, we create a waveguide width profile $w(z)$ along the optical axis and map this into a dispersive effective index profile $n_{\mathrm{eff}}(z,\lambda) = n_{\mathrm{eff}}(\lambda) + \mathrm{d}n(z) + i*k$, where $n_{\mathrm{eff}}(\lambda)$ accounts for the waveguide dispersion, $\mathrm{d}n(z)$ accounts for the sidewall modulation (empirically scaled down by 2.3 for the best agreement between our 1D approximation and real 3D nanowires as in ref 41), and the imaginary component k accounts for the nominal propagation loss (∼2.5 dB/cm) of a standard nanowire. This is performed for both type-A and type-B structures. Sequential waveguide segments with the same width are clustered to improve simulation time. Group index calculation: We determine the group index of finite-length crystals using the transfer matrix method and numerically solving for the density of modes (DOM). The DOM, $\frac{\mathrm{d}k}{\mathrm{d}\omega}$, and therefore c/n_g are extracted from the spectral response of the complex transmission coefficient as described in ref 39. CD bias-corrected device modeling: We find that due to CD bias, there is a discrepancy between the initially designed/simulated structures and the fabricated structures. To account for the realized CD bias, we apply an "initial" bias correction by reducing the waveguide widths in our model to match the fabricated structures. However, this step alone is not sufficient for the type-B structures. To obtain better agreement between the experiment and our model for type-B devices, we apply an "advanced" bias correction, which reduces both the width and length of the narrow grating teeth as observed in the SEM image of Figure 2e. More details regarding the advanced bias and its comparison to the initial model are provided in Figure S6.

Experiment. Devices were fabricated using the NanoSOI MPW fabrication process by Applied Nanotools, Inc. (http://www.appliednt.com/nanosoi; Edmonton, Canada) and measured at The University of British Columbia through the Silicon Electronic-Photonic Integrated Circuits program.[42] Silicon-on-insulator wafers of 200 mm diameter, 220 nm device thickness, and 2 μm buffer oxide thickness are used as the base material for the fabrication. Devices were patterned in hydrogen silsesquioxane (HSQ) resist using a Raith EBPG 5000+ electron beam instrument with a raster step size of 5 nm. The exposure dosage of the design was corrected for proximity effects that result from the backscatter of electrons from exposure of nearby features. After development, a chlorine-based anisotropic ICP-RIE etch process was performed to etch the silicon device layer. SEM inspection was performed after stripping the remaining resist with a 10:1 buffer oxide wet etch, followed by plasma-enhanced chemical vapor deposition (PECVD) of an ∼2.2 μm thick oxide top cladding layer based on tetraethyl orthosilicate (TEOS) at 300 °C. Following fabrication, grating-coupled transmission spectra were collected under TE polarization using a tunable laser (Agilent 81600B) and an optical power meter (Agilent 81635A) over the range 1500−1600 nm in 10 pm steps.

ASSOCIATED CONTENT

Supporting Information

The Supporting Information is available free of charge at https://pubs.acs.org/doi/10.1021/acsphotonics.1c01800.

Experimental transmission spectra of silicon photonic Bragg mirrors with a period skew of 317−324 nm; comparison of the type-A (asymmetric) and type-B (symmetric) moiré lattice; transmission spectra; group indices for varying crystal lengths; simulated transmission spectra for initial and advanced bias; and theoretical model of transmission characteristics of the initial phase-modulated type-A moiré structures (PDF)

AUTHOR INFORMATION

Corresponding Author

Judson D. Ryckman − *Holcombe Department of Electrical and Computer Engineering, Clemson University, Clemson, South Carolina 29634, United States;* orcid.org/0000-0001-8125-099X; Email: jryckma@clemson.edu

Authors

Tahmid H. Talukdar − *Holcombe Department of Electrical and Computer Engineering, Clemson University, Clemson, South Carolina 29634, United States;* orcid.org/0000-0002-3664-716X

Anna L. Hardison − *Holcombe Department of Electrical and Computer Engineering, Clemson University, Clemson, South Carolina 29634, United States*

Complete contact information is available at: https://pubs.acs.org/10.1021/acsphotonics.1c01800

Funding

This work was supported in part by the National Science Foundation (CMMI-1825787) and the Air Force Office of Scientific Research (AFOSR) Young Investigator Research Program (FA9550-19-1-0057).

Notes

The authors declare no competing financial interest.

ACKNOWLEDGMENTS

The authors acknowledge the edX UBCx Phot1x Silicon Photonics Design, Fabrication and Data Analysis course organized by Lukas Chrostowski, which is supported by the Natural Sciences and Engineering Research Council of Canada (NSERC) Silicon Electronic-Photonic Integrated Circuits (SiEPIC) Program; Cameron Horvath of Applied NanoTools, Inc. for device fabrication; and Iman Taghavi for performing semiautomated measurements at The University of British Columbia.

REFERENCES

(1) Carr, S.; Massatt, D.; Fang, S.; Cazeaux, P.; Luskin, M.; Kaxiras, E. Twistronics: Manipulating the Electronic Properties of Two-Dimensional Layered Structures through Their Twist Angle. *Phys. Rev. B* **2017**, *95*, No. 075420.

(2) Cao, Y.; Fatemi, V.; Fang, S.; Watanabe, K.; Taniguchi, T.; Kaxiras, E.; Jarillo-Herrero, P. Unconventional Superconductivity in Magic-Angle Graphene Superlattices. *Nature* **2018**, *556*, 43−50.

(3) Brem, S.; Linderälv, C.; Erhart, P.; Malic, E. Tunable Phases of Moiré Excitons in van Der Waals Heterostructures. *Nano Lett.* **2020**, *20*, 8534−8540.
(4) Cao, Y.; Luo, J. Y.; Fatemi, V.; Fang, S.; Sanchez-Yamagishi, J. D.; Watanabe, K.; Taniguchi, T.; Kaxiras, E.; Jarillo-Herrero, P. Superlattice-Induced Insulating States and Valley-Protected Orbits in Twisted Bilayer Graphene. *Phys. Rev. Lett.* **2016**, *117*, No. 116804.
(5) Sharpe, A. L.; Fox, E. J.; Barnard, A. W.; Finney, J.; Watanabe, K.; Taniguchi, T.; Kastner, M. A.; Goldhaber-Gordon, D. Emergent Ferromagnetism near Three-Quarters Filling in Twisted Bilayer Graphene. *Science* **2019**, *365*, 605−608.
(6) Zhang, Q.; Hu, G.; Ma, W.; Li, P.; Krasnok, A.; Hillenbrand, R.; Alù, A.; Qiu, C. W. Interface Nano-Optics with van Der Waals Polaritons. *Nature* **2021**, *597*, 187−195.
(7) Hu, G.; Ou, Q.; Si, G.; Wu, Y.; Wu, J.; Dai, Z.; Krasnok, A.; Mazor, Y.; Zhang, Q.; Bao, Q.; Qiu, C. W.; Alù, A. Topological Polaritons and Photonic Magic Angles in Twisted α-MoO3 Bilayers. *Nature* **2020**, *582*, 209−213.
(8) Oudich, M.; Su, G.; Deng, Y.; Benalcazar, W.; Huang, R.; Gerard, N. J. R. K.; Lu, M.; Zhan, P.; Jing, Y. Photonic Analog of Bilayer Graphene. *Phys. Rev. B* **2021**, *103*, No. 214311.
(9) Wang, P.; Zheng, Y.; Chen, X.; Huang, C.; Kartashov, Y. V.; Torner, L.; Konotop, V. V.; Ye, F. Localization and Delocalization of Light in Photonic Moiré Lattices. *Nature* **2020**, *577*, 42−46.
(10) Fu, Q.; Wang, P.; Huang, C.; Kartashov, Y. V.; Torner, L.; Konotop, V. V.; Ye, F. Optical Soliton Formation Controlled by Angle Twisting in Photonic Moiré Lattices. *Nat. Photonics* **2020**, *14*, 663−668.
(11) Mao, X. R.; Shao, Z. K.; Luan, H. Y.; Wang, S. L.; Ma, R. M. Magic-Angle Lasers in Nanostructured Moiré Superlattice. *Nat. Nanotechnol.* **2021**, *16*, 1099−1105.
(12) Wang, W.; Gao, W.; Chen, X.; Shi, F.; Li, G.; Dong, J.; Xiang, Y.; Zhang, S. Moiré Fringe Induced Gauge Field in Photonics. *Phys. Rev. Lett.* **2020**, *125*, No. 203901.
(13) Lassaline, N.; Brechbühler, R.; Vonk, S. J. W.; Ridderbeek, K.; Spieser, M.; Bisig, S.; le Feber, B.; Rabouw, F. T.; Norris, D. J. Optical Fourier Surfaces. *Nature* **2020**, *582*, 506−510.
(14) Hu, G.; Krasnok, A.; Mazor, Y.; Qiu, C. W.; Alù, A. Moiré Hyperbolic Metasurfaces. *Nano Lett.* **2020**, *20*, 3217−3224.
(15) Han, J.-H.; Kim, I.; Ryu, J.-W.; Kim, J.; Cho, J.-H.; Yim, G.-S.; Park, H.-S.; Min, B.; Choi, M. Rotationally Reconfigurable Metamaterials Based on Moiré Phenomenon. *Opt. Express* **2015**, *23*, 17443.
(16) Lubin, S. M.; Hryn, A. J.; Huntington, M. D.; Engel, C. J.; Odom, T. W. Quasiperiodic Moiré Plasmonic Crystals. *ACS Nano* **2013**, *7*, 11035−11042.
(17) Aubry, S.; Andre, G. Analyticity Breaking and Anderson Localization in Incommensurate Lattices. *Ann. Isr. Phys. Soc.* **1980**, *3*, 133−140.
(18) Harper, P. G. Single Band Motion of Conduction Electrons in a Uniform Magnetic Field. *Proc. Phys. Soc., Sect. A* **1955**, *68*, 874−878.
(19) Cheng, R.; Jaeger, N. A. F.; Chrostowski, L. Fully Tailorable Integrated-Optic Resonators Based on Chirped Waveguide Moiré Gratings. *Optica* **2020**, *7*, 647−657.
(20) Simbula, A.; Schatzl, M.; Zagaglia, L.; Alpeggiani, F.; Andreani, L. C.; Schäffler, F.; Fromherz, T.; Galli, M.; Gerace, D. Realization of High-Q/v Photonic Crystal Cavities Defined by an Effective Aubry-André-Harper Bichromatic Potential. *APL Photonics* **2017**, *2*, No. 056102.
(21) Combrié, S.; Lehoucq, G.; Moille, G.; Martin, A.; De Rossi, A. Comb of High-Q Resonances in a Compact Photonic Cavity. *Laser Photonics Rev.* **2017**, *11*, No. 1700099.
(22) Marty, G.; Combrié, S.; Raineri, F.; De Rossi, A. Photonic Crystal Optical Parametric Oscillator. *Nat. Photonics* **2021**, *15*, 53−58.
(23) Bin Tarik, F.; Famili, A.; Lao, Y.; Ryckman, J. D. Robust Optical Physical Unclonable Function Using Disordered Photonic Integrated Circuits. *Nanophotonics* **2020**, *9*, 2817−2828.
(24) Strain, M. J.; Thoms, S.; MacIntyre, D. S.; Sorel, M. Multi-Wavelength Filters in Silicon Using Superposition Sidewall Bragg Grating Devices. *Opt. Lett.* **2014**, *39*, No. 413.
(25) Alpeggiani, F.; Andreani, L. C.; Gerace, D. Effective Bichromatic Potential for Ultra-High Q-Factor Photonic Crystal Slab Cavities. *Appl. Phys. Lett.* **2015**, *107*, No. 261110.
(26) Wang, X.; Wang, Y.; Flueckiger, J.; Bojko, R.; Liu, A.; Reid, A.; Pond, J.; Jaeger, N. A. F.; Chrostowski, L. Precise Control of the Coupling Coefficient through Destructive Interference in Silicon Waveguide Bragg Gratings. *Opt. Lett.* **2014**, *39*, 5519−5522.
(27) Liu, S.; Shi, Y.; Zhou, Y.; Zhao, Y.; Zheng, J.; Lu, J.; Chen, X. Planar Waveguide Moiré Grating. *Opt. Express* **2017**, *25*, 24960−24973.
(28) Alemohammad, H. *Opto-Mechanical Fiber Optic Sensors - Research, Technology, and Applications in Mechanical Sensing*; Elsevier, 2018.
(29) Liu, J.-M. *Photonic Devices*; Cambridge University Press, 2005.
(30) Li, Q.; Wang, T.; Su, Y.; Yan, M.; Qiu, M. Coupled Mode Theory Analysis of Mode-Splitting in Coupled Cavity System. *Opt. Express* **2010**, *18*, 8367.
(31) Quan, Q. M.; Loncar, M. Deterministic Design of Wavelength Scale, Ultra-High Q Photonic Crystal Nanobeam Cavities. *Opt. Express* **2011**, *19*, 18529.
(32) Chan, J.; Eichenfield, M.; Camacho, R.; Painter, O. Optical and Mechanical Design of a "Zipper" Photonic Crystal Optomechanical Cavity. *Opt. Express* **2009**, *17*, 3802−3819.
(33) Clementi, M.; Barone, A.; Fromherz, T.; Gerace, D.; Galli, M. Selective Tuning of Optical Modes in a Silicon Comb-like Photonic Crystal Cavity. *Nanophotonics* **2019**, *9*, 205−210.
(34) Yariv, A.; Xu, Y.; Lee, R. K.; Scherer, A. Coupled-Resonator Optical Waveguide: A Proposal and Analysis. *Opt. Lett.* **1999**, *24*, 711−713.
(35) Stefanou, N.; Modinos, A. Impurity Bands in Photonic Insulators. *Phys. Rev. B* **1998**, *57*, 12127−12133.
(36) Lian, J.; Sokolov, S.; Yüce, E.; Combrié, S.; De Rossi, A.; Mosk, A. P. Dispersion of Coupled Mode-Gap Cavities. *Opt. Lett.* **2015**, *40*, No. 4488.
(37) Yamilov, A. G.; Herrera, M. R.; Bertino, M. F. Slow-Light Effect in Dual-Periodic Photonic Lattice. *J. Opt. Soc. Am. B* **2008**, *25*, No. 599.
(38) Altug, H.; Vučković, J. Two-Dimensional Coupled Photonic Crystal Resonator Arrays. *Appl. Phys. Lett.* **2004**, *84*, 161−163.
(39) Bendickson, J. M.; Dowling, J. P.; Scalora, M. Analytic Expressions for the Electromagnetic Mode Density in Finite, One-Dimensional, Photonic Band-Gap Structures. *Phys. Rev. E* **1996**, *53*, 4107−4121.
(40) Ohta, K.; Ishida, H. Matrix Formalism for Calculation of Electric Field Intensity of Light in Stratified Multilayered Films. *Appl. Opt.* **1990**, *29*, 1952−1959.
(41) Cheng, R.; Han, Y.; Chrostowski, L. Characterization and Compensation of Apodization Phase Noise in Silicon Integrated Bragg Gratings. *Opt. Express* **2019**, *27*, 9516−9535.
(42) Chrostowski, L.; Shoman, H.; Hammood, M.; Yun, H.; Jhoja, J.; Luan, E.; Lin, S.; Mistry, A.; Witt, D.; Jaeger, N. A. F.; Shekhar, S.; Jayatilleka, H.; Jean, P.; Villers, S. B-.; Cauchon, J.; Shi, W.; Horvath, C.; Westwood-Bachman, J. N.; Setzer, K.; Aktary, M.; Patrick, N. S.; Bojko, R. J.; Khavasi, A.; Wang, X.; de Lima, T. F.; Tait, A. N.; Prucnal, P. R.; Hagan, D. E.; Stevanovic, D.; Knights, A. P. Silicon Photonic Circuit Design Using Rapid Prototyping Foundry Process Design Kits. *IEEE J. Sel. Top. Quantum Electron.* **2019**, *25*, 1−26.

https://doi.org/10.1021/acsphotonics.1c01800
ACS Photonics 2022, 9, 1286−1294